AGU PUBLICATIONS

JGR

Journal of Geophysical Research: Solid Earth

RESEARCH ARTICLE
10.1002/2017JB014592

Key Points:
- A tomography study reveals subsurface geometry of the Lusi region and the neighboring volcanic complex
- A >6 km deep hydrothermal plume reaches the surface at Lusi
- Magma chambers imaged below the volcanic complex connect with the Lusi conduit; the Lusi active system is fed by the volcanic arc activity

Supporting Information:
- Supporting Information S1
- Figure S1
- Figure S2

Correspondence to:
A. Mazzini,
adriano.mazzini@geo.uio.no

Citation:
Fallahi, M. J., Obermann, A., Lupi, M., Karyono, K., & Mazzini, A. (2017). The plumbing system feeding the Lusi eruption revealed by ambient noise tomography. *Journal of Geophysical Research: Solid Earth*, *122*, 8200–8213. https://doi.org/10.1002/2017JB014592

Received 21 JUN 2017
Accepted 23 SEP 2017
Accepted article online 17 OCT 2017
Published online 28 OCT 2017

The Plumbing System Feeding the Lusi Eruption Revealed by Ambient Noise Tomography

Mohammad Javad Fallahi[1], Anne Obermann[2], Matteo Lupi[3], Karyono Karyono[1,4,5], and Adriano Mazzini[1]

[1]Centre for Earth Evolution and Dynamics (CEED), University of Oslo, Oslo, Norway, [2]Swiss Seismological Service, ETH Zürich, Zürich, Switzerland, [3]Department of Earth Sciences, University of Geneva, Geneva, Switzerland, [4]Faculty of Engineering Geology, Padjadjaran University (UNPAD), Bandung, Indonesia, [5]Centre for Earthquake and Tsunami, Agency for Meteorology, Climatology and Geophysics (BMKG), Jakarta, Indonesia

Abstract Lusi is a sediment-hosted hydrothermal system featuring clastic-dominated geyser-like eruption behavior in East Java, Indonesia. We use 10 months of ambient seismic noise cross correlations from 30 temporary seismic stations to obtain a 3-D model of shear wave velocity anomalies beneath Lusi, the neighboring Arjuno-Welirang volcanic complex, and the Watukosek fault system connecting the two. Our work reveals a hydrothermal plume, rooted at a minimum 6 km depth that reaches the surface at the Lusi site. Furthermore, the inversion shows that this vertical anomaly is connected to the adjacent volcanic complex through a narrow (~3 km wide) low velocity corridor slicing the survey area at a depth of ~4–6 km. The NE-SW direction of this elongated zone matches the strike of the Watukosek fault system. Distinct magmatic chambers are also inferred below the active volcanoes. The large-scale tomography features an exceptional example of a subsurface connection between a volcanic complex and a solitary erupting hydrothermal system hosted in a hydrocarbon-rich back-arc sedimentary basin. These results are consistent with a scenario where deep-seated fluids (e.g., magmas and released hydrothermal fluids) flow along a region of enhanced transmissivity (i.e., the Watukosek fault system damage zone) from the volcanic arc toward the back arc basin where Lusi resides. The triggered metamorphic reactions occurring at depth in the organic-rich sediments generated significant overpressure and fluid upwelling that is today released at the spectacular Lusi eruption site.

Plain Language Summary The Lusi mud eruption started the 26 May 2006 in the northeast of Java, Indonesia. More than 11 years later Lusi is still active and continuously erupting boiling mud, rock fragments, gas, and water with stunning flow rates that reached up to 180.000 m^3/d. Today Lusi occupies a 7 km^2 area framed by tall embankment walls that prevent a broader expansion of the mudflows. This spectacular eruption site has been investigated by numerous studies; however, images of the deep plumbing system are still missing. Here we present the result of a broad ambient noise tomography survey aiming to image the subsurface of the Lusi eruption site, the neighboring volcanic complex, and the faulted region that connects these two structures. Results show the presence of a >6 km deep hydrothermal plume below Lusi. The magma chamber imaged below the volcanic complex connects with the Lusi conduit through an elongated corridor that is oriented following the fault direction. Our results support a scenario where the Lusi eruption is fed at depth by the migration of fluids originating from the volcanic complex interacting with the organic-rich sediments present at 4.5 km depth.

1. Introduction

Since 29 May 2006, the densely populated Sidoarjo district, located in the NE of the Java sedimentary basin, has witnessed the extensive eruption of boiling mud, clasts, and fluids (Miller & Mazzini, 2017; Van Noorden, 2006). The large scale of the mud eruption, nicknamed Lusi, significantly impacted this area with nearly 60,000 people forced to abandon their villages due to the hot erupting mud covering a region of ~7 km^2 (Richards, 2011). The eruption site reached flow rates of up to 180.000 m^3/d (Mazzini et al., 2007) and currently (February 2017) in the order of 80.000 m^3/d. Lusi is a unique system on Earth due to its longevity and has been studied extensively over the past decade with geological investigations (Davies et al., 2008; Istadi et al., 2009; Mazzini et al., 2007; Sawolo et al., 2009; Tanikawa et al., 2010; Tingay et al., 2008), geochemical and experimental approaches (Mazzini et al., 2017, 2012; Vanderkluysen et al., 2014),

geophysical methods (Karyono et al., 2017; Manga et al., 2009; Mauri, Husein, Mazzini, Irawan, et al., 2017; Mauri, Husein, Mazzini, Karyono, et al., 2017; Obermann et al., 2017; Shirzaei et al., 2015), and numerical studies (Collignon et al., 2017; Lupi et al., 2013; Lupi et al., 2014; Mazzini et al., 2009; Rudolph et al., 2011; Sohrabi et al., 2017; Svensen et al., 2017). However, despite the numerous studies, several questions remain unanswered. In particular, the geometry of the deep feeding system remains uncertain. Large-scale geophysical methods are a viable tool to investigate this aspect.

Seismic tomography is a powerful tool to explore the velocity structure of the upper lithosphere (Nolet, 1987; Tromp et al., 2005). Using this technique along with dense seismic networks, it is possible to identify high- and low-velocity zones associated with geological phenomena and structures such as hydrothermal systems (Obermann et al., 2016), magmatic bodies (Koulakov et al., 2009; Koulakov & Shapiro, 2015), mud volcanoes (Koulakov et al., 2017), and ore deposits (Olivier et al., 2015). Piercement structures (such as Lusi) are geological phenomena driven also by the development of elevated pore pressure and fluid migration at depth. Fluid accumulations and migrations in the upper crust may result in the development of shear wave anomalies. Mapping such anomalies assists with identifying the occurrence (and eventually the broad geometry) of such reservoirs (De Matteis et al., 2010; Jaxybulatov et al., 2014; Vanorio et al., 2005).

Due to the lack of significant local seismicity in the region (Obermann et al., 2017), local earthquake tomography methods (Kissling, 1988; Koulakov & Shapiro, 2015; Thurber, 1983) could not be applied to investigate the subsurface velocity variations in the area below Lusi and the neighboring volcanic complex. A viable tool that has provided excellent results, also in volcanic environments, is ambient noise tomography (ANT) (Brenguier et al., 2007; Jaxybulatov et al., 2014; Luzón et al., 2011; Masterlark et al., 2010; Mordret et al., 2014; Obermann et al., 2016; Stankiewicz et al., 2010; Villagómez et al., 2011). The ANT method inverts dispersive surface waves across station pairs using long-lasting records of seismic noise (Campillo & Paul, 2003; Claerbout, 1968; Lobkis & Weaver, 2001; Shapiro & Campillo, 2004). The method assumes that the cross-correlation function (CC) represents an approximation of the Green's function between receiver-pairs. From there, group (or phase) velocity maps can be constructed (Ritzwoller et al., 2011; Shapiro et al., 2005). Brenguier et al. (2007), Stankiewicz et al. (2010), and Obermann et al. (2016) have shown that shear wave velocity anomalies inverted from group velocity maps are capable of pointing out the occurrence of fluid-rich geological compartments in the upper crust.

Tomographic images of upper crust beneath central and east Java were previously constructed by ANT on a larger regional scale (Martha et al., 2017; Zulfakriza et al., 2014). We completed an ANT study using the data collected by a dense network of 30 seismometers distributed over an area of more than 1,000 km^2 (Figure 1). This is the first study that provides a local high resolution tomographic model of the area. The goal of this study was to address the following questions: how deep is the source of fluids feeding the Lusi eruption site? How are Lusi and the feeding volcanic complex interconnected at depth?

2. Geological Setting and Lusi Plumbing System

The NE Java basin is a back-arc hydrocarbon province that hosts a large variety of buried and exposed piercement structures as well as deep-reaching strike-slip fault systems (Situmorang et al., 1976; Satyana & Asnidar, 2008; Istadi et al., 2009; Mazzini et al., 2009). Piercements are also present in the southern part of the basin, in the proximity of the volcanic arc (Istadi et al., 2012). Lusi is the most spectacular ongoing clastic eruption on Earth located just a few kilometers from the Arjuno Welirang volcanic complex.

The region where Lusi resides is connected to the Arjuno Welirang complex by the Watukosek fault system (WFS) (Figure 1). This left-lateral strike-slip fracture zone originates from the youngest cone of the complex (i.e., Penanggungan) and extends toward the NE of Java, where a ~160 m high escarpment crops out (Watukosek escarpment). The fault system continues toward the NE, intersecting Lusi and several other mud volcanoes.

Mazzini et al. (2009, 2012) suggested that the WFS is key to understand fluid flow dynamics of the East Java basin as it may focus the migration of magmas and deep fluids from the active volcanic arc toward the back-arc basin where Lusi resides. This results in the elevated geothermal gradient of the southern part of the basin where kerogens and/or already existing hydrocarbon maturation are enhanced (Mazzini et al., 2007). These conditions commonly lead to the development of piercement structures rooted at overpressured and organic-rich sedimentary units (Mazzini & Etiope, 2017).

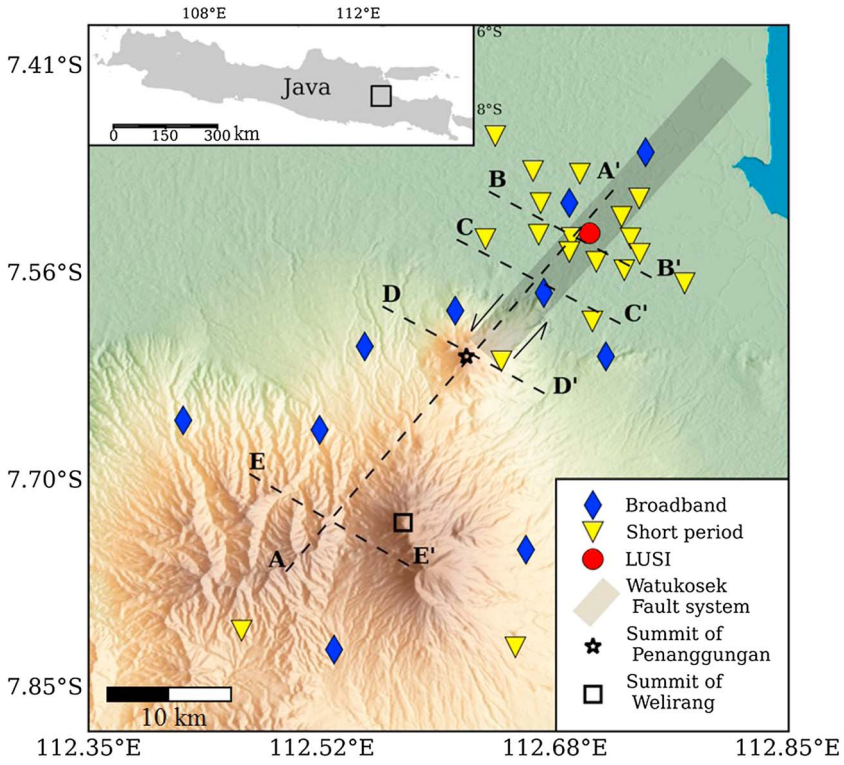

Figure 1. Topographic map showing the network distribution in the East Java Basin and pointing out the main geological features of the study area. Seismic station locations are marked by yellow triangles (short period) and blue diamonds (broadband). The red circle indicates Lusi. Summit of Penanggungan volcano is marked by a black star symbol and summit of Welirang volcano by a black square. The black dashed lines denote the location of the vertical slices through the 3-D shear wave velocity model that are shown in Figure 9.

Surface modeling deformation recorded by InSAR (Shirzaei et al., 2015) recently confirmed that Lusi is fed by two distinct regions located at approximately 1.5 km and >4 km depth. These regions correspond to two fluid sources that were distinguished by geochemical analysis (Mazzini et al., 2007, 2012, 2017). Furthermore, a magmatic source feeding the Lusi system with intense crustal fluid flow, upwelling from depth, has been put forward based on observations of the eruptive activity coupled with seismic data (Karyono et al., 2017; Vanderkluysen et al., 2014). The hot (~100°C) erupted fluids have a geochemical composition that clearly shows a component of mantellic origin mixed with fluids originating from metamorphic reactions at temperatures that are higher than the local gradient (Mazzini et al., 2012, 2017). For these reasons, the authors pointed out that Lusi is a sediment-hosted hydrothermal system fed by a vigorous hydrothermal circulation, most likely related to the neighboring volcanic complex. Besides the obvious geochemical evidence, a clear subsurface image of the link between the deep-seated reservoirs fuelling Lusi and the neighboring volcanic arc remains missing. For these reasons, we specifically designed a large-scale seismic experiment aimed at revealing the subsurface fluid distribution upon which Lusi develops.

3. Ambient Noise Tomography

3.1. Seismic Data and Computation of Cross Correlations

From January 2015 to November 2016, a network including 10 broadband (Guralp CMG3T sensors in combination with EarthData Loggers) and 20 short-period seismic sensors (15 1 s LE-3Dlite Lennartz with Nanometrics digitizer and 5 Mark L-4-3D sensors with EDL) was deployed around the Arjuno Welirang volcanic complex, the WFS, and the Lusi eruption site (Figure 1). The data set used in this study was collected within the framework of the ERC LusiLab project and considered the vertical component of the first 10 months of continuously recorded seismic data.

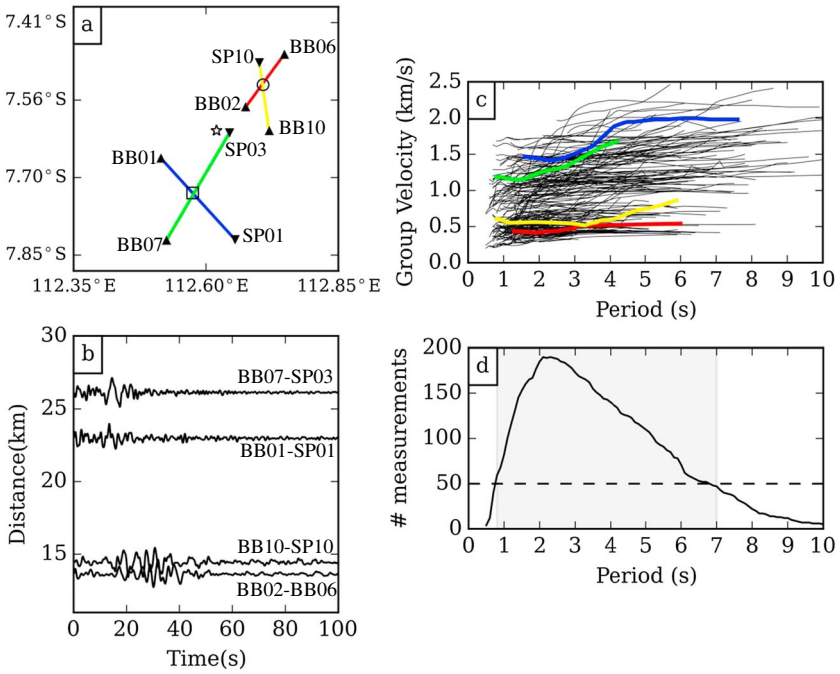

Figure 2. Group velocity dispersion measurement. (a) Ray paths crossing different parts of the study area with high and low velocities. (b) CCs for the raypaths in Figure 2a indicating lower velocities and stronger dispersion in the area of Lusi. (c) All measured group velocity dispersion curves. The four colored dispersion curves correspond to raypaths in Figure 2a. (d) Number of group velocities at each period. The horizontal dashed line indicates the minimum number of group velocity measurements being considered for tomography.

To build up a database of noise cross-correlation functions (CCs) we first slice daily records into 2 h length segments and then apply the following processing steps: correction of the instrumental response, resampling the data to 10 Hz, band pass-filtering between 0.05 and 4 Hz, elimination of 2 h length segments with standard deviations more than 3 times the standard deviation of a daily record, spectral whitening from 0.05 to 4 Hz, and one-bit amplitude normalization. We then calculate the CCs between all station pairs for the remaining 2 h segments and stack them over the 10 months. Noise sources are not homogeneously distributed and originate predominantly from coastlines; therefore, CCs between a couple of station pairs are asymmetric. We average the waveforms at positive and negative lag times to enhance the part of the signal that is symmetric and increase the signal-to-noise ratio (e.g., Mordret et al., 2015). Figures 2a and 2b provide a comparison of raypaths crossing the eruption site and the volcanic complex. Lower velocities and stronger dispersion can be observed on paths crossing the Lusi eruption site.

3.2. Group Velocity Dispersion Curves

From the CCs between each station pair, we obtain the group velocity dispersion curves using a narrow bandpass multiple-filtering analysis following the method of Levshin et al. (1989). We use a graphical user interface that involves analyst validation of the dispersion curves and the possibility to manually pick them (Mordret et al., 2014). To identify and reject unreliable group velocity measurements, we use only the CCs that have a signal-to-noise ratio equal to or larger than 10 and an interstation distance of more than 1.5 wavelengths. All measured dispersion curves are plotted in Figure 2c. We observe a cluster of low-velocity dispersion curves (0.3–0.6 km/s) and a broader range of relatively flat dispersion curves with velocities from 0.8 to 1.7 km/s. Figure 2d shows the number of measurements per period. We limit our analysis to periods with at least 50 measurements, which restricts our study to the period range comprised between 1 s and 7 s.

3.3. 2-D Group Velocity Tomography

An iterative nonlinear tomographic inversion procedure (fast marching surface wave tomography) developed by Rawlinson and Sambridge (2005) is used to obtain tomographic images of lateral group-velocity variations. The code uses a grid-based eikonal solver (Rawlinson & Sambridge, 2005; Sethian, 1996; Sethian &

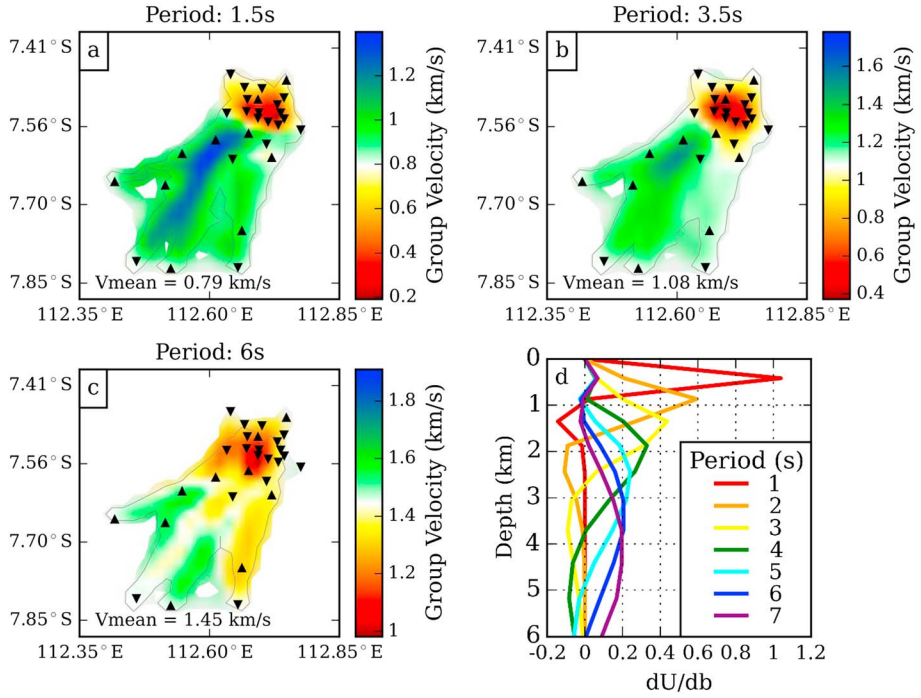

Figure 3. Group velocity maps. Group velocity maps at (a) 1.5 s, (b) 3.5 s, and (c) 6 s. The values of mean surface wave velocity are shown on the bottom of each map. The light gray contours indicate regions with more than four rays per cell. The black triangles denote the seismic station locations. (d) Depth sensitivity kernels for surface wave group velocities at a set of periods from 1 s to 7 s.

Popovici, 1999) for the forward prediction of surface wave travel times and solves the inverse problem using a subspace inversion scheme (Kennett et al., 1988).

The study area (Figure 1) is discretized into 24 × 24 squared grid cells of 0.02° (~2.3 km) length each. We compute 2-D group velocity maps for a discrete set of periods from 1 s to 7 s with steps of 0.1 s. The overall mean surface wave velocity at each period is used as the constant starting velocity model for the tomographic inversion. The standard deviation computed from the total number of travel times at each period is considered as an uncertainty measurement associated to each interstation travel time. The topography is not taken into account during the inversion procedure, which can induce errors of less than 5% in areas with a high topographic gradient (Brenguier et al., 2007; Mordret et al., 2015), that is, below the volcanic arc.

Figures 3a–3c show examples of 2-D group velocity maps at 1.5 s, 3.5 s, and 6 s periods, where surface waves are sensitive to structures shallower than approximately 6 km in depth (Figure 3d). Only areas with a ray coverage above 4 per cell are displayed (Figure 4). Extremely low velocities (e.g., 200 m/s at period of 1.5 s) are observed at the Lusi location for every period. At greater depths (i.e., 6 s, Figure 3c) the low velocity area extends toward the volcanic complex. Close to the surface (Figure 3a), we observe a high velocity anomaly below the volcanic complex that is elongated in NE-SW direction.

To determine the robustness of the 2-D tomographic results we investigate the raypath density (Figure 4) and the spatial resolution capacities of the inversion (Figures 5 and 6). Figures 4a–4c show the dispersion measurements at periods of 1.5 s, 3.5 s, and 6 s plotted in map view and color-coded based on the measured group velocities for each station pair. The black contour outlines the regions with more than four rays per cell used in the inversion. Corresponding ray densities are shown in Figures 4d–4f. As expected from the network geometry, we have dense ray coverage around Lusi with good azimuthal distribution. Toward the volcanic chain the coverage is less dense and most raypaths have a NE-SW orientation. This introduces a smearing effect in this direction, and additionally, the path density decreases with increasing period. To quantify the lateral smearing, we performed a spike test (Mordret et al., 2015) at different frequencies (Figure 5). In Figure 5a we see three input spikes at different locations (A: Lusi, B: the Penanggungan volcano, C: the Southern extent of the Arjuno Welirang volcanic complex). In Figures 5b–5d we see the reconstructed

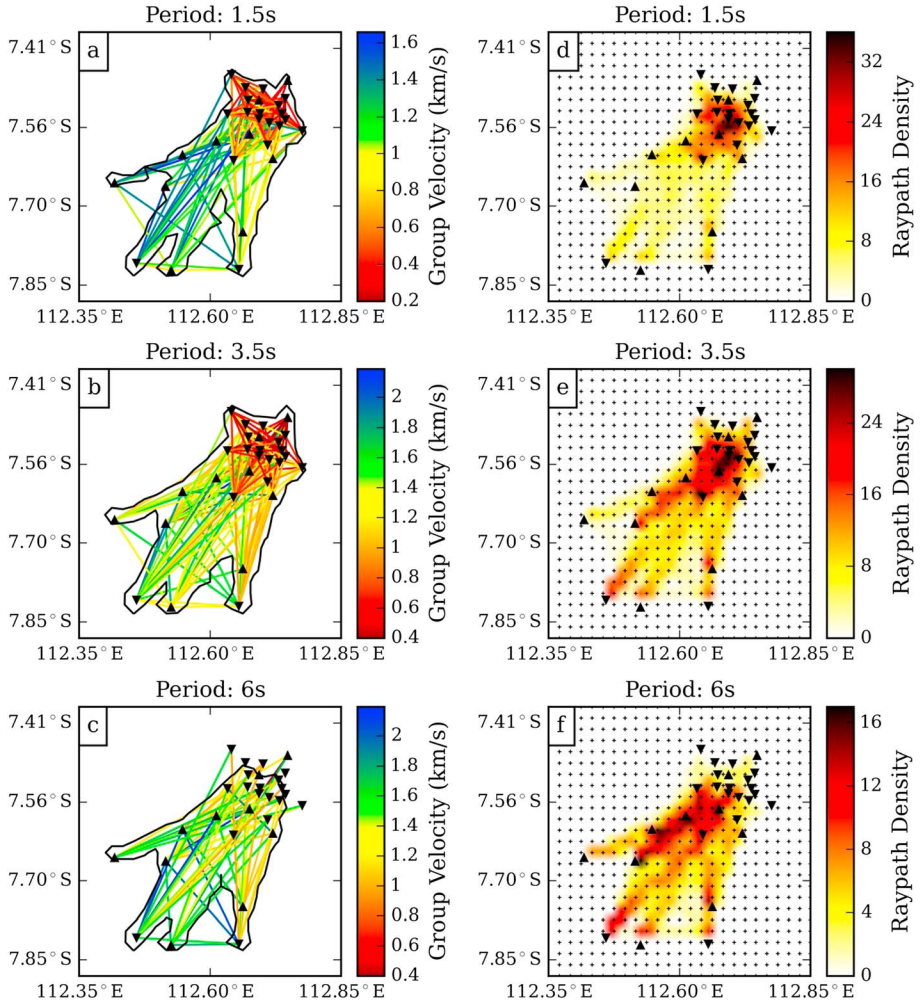

Figure 4. Ray path coverage. Color-coded raypaths showing group velocity measurements at (a) 1.5 s, (b) 3.5 s, and (c) 6 s. The black contours frame regions with more than four rays per cell. The black triangles denote the seismic station locations. Number of paths crossing each cell for (d) 1.5 s, (e) 3.5 s, and (f) 6 s.

spike anomalies at different frequencies. While the anomalies below Lusi and Penanggungan volcano (A and B) can be seen in good resolution, we observe a significant smearing of the anomalies across the SW part of the complex. Figures 6a–6c show the displacement per cell at the centers of the input spikes after inversion, the so-called resolution shift. An anomaly is well located if the resolution shift is about half the cell size, which corresponds here to 1.2 km. We observe again that the area around Lusi until the Penanggungan volcano is seen in good resolution, whereas significant shifts of up to 12 km occur toward the SW in the region around Welirang volcano cone. Figures 6d–6f show the resolution for the entire area using spike type anomalies (Barmin et al., 2001; Mordret et al., 2013; Obermann et al., 2016).

3.4. Depth Inversion

From the group velocity maps we can construct dispersion curves for each grid point. We use a neighborhood algorithm (Sambridge, 1999) to invert the constructed local dispersion curves for the 1-D velocity structure at each grid point. 1-D Vs profiles are built as a power law with 15 homogeneous isotropic layers overlaid by Vs anomalies. Shear velocity at each layer is controlled by surface velocity in the range of 200–1,400 m/s and curvature of the profile in the range of 0.1–0.3 (see Figure 10 in Mordret et al., 2015 for details of these parameters). Velocity perturbations in the range of ±30% are added to each layer in respect to the previous layer. These perturbations allow the algorithm to generate Vs profiles with small velocity variations/slight decrease at depth and give a much higher level of fit to areas around the eruption site and volcanoes.

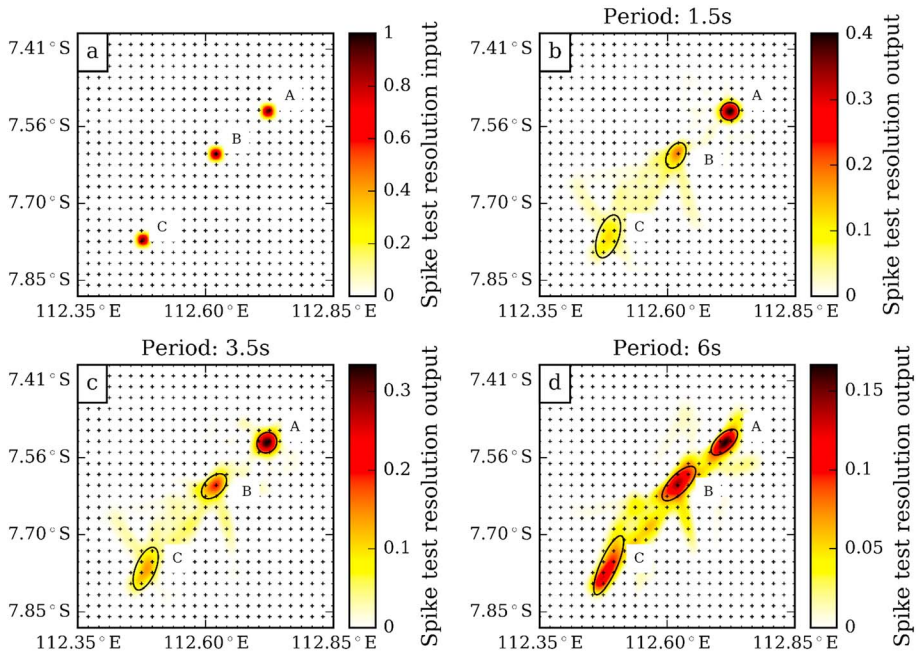

Figure 5. Synthetic spike test. (a) Input spikes at three different locations. Reconstructed spike anomalies at (b) 1.5 s, (c) 3.5 s, and (d) 6 s. The black contours are the contour levels at 40% of the maximum amplitude of the output spike.

Surface waves are more sensitive to Vs than Vp; therefore, only Vs is inverted and Vp is updated using the Poisson's ratio. At the same time, density is calculated from the new Vp using $\rho(g/cm^3)$ = (Vp(km/s) + 2.37)/2.81 (Gebrande, 1982). The algorithms are described in detail in Mordret et al. (2014). We sample a total of 11,000 Vs models per grid cell (Figure 7b). The average over the best 1,000 models is used to construct the 3-D velocity models. For each point of the grid, the misfit of the used 1-D model is $<$0.3.

The results of the depth inversion are presented in the form of horizontal and vertical slices in Figures 8 and 9, respectively. The standard deviations of the best 1,000 models for each grid cell are used to construct the uncertainty 3-D model and are presented as equivalent of Figures 8 and 9 (Figures S1 and S2 in the supporting information). Vs uncertainties increase with depth and reach values larger than 0.15 km/s in some grid cells. However, uncertainties remain $<$0.1 km/s, where we show the results on vertical slices; thus, this does not affect our geological interpretations. The exact position of the vertical slices is marked in Figure 1. We have a good resolution up to a depth of 6 km. Close to the surface (Figure 8a), we observe a significant low velocity anomaly of 20% below Lusi and the surrounding area (10 km $\times$ 15 km). The vertical cross section (Figures 9a and 9b) reveals that this anomaly persists to a depth of 1.5 km. It then narrows down to approximately 4 km in width and is still present at 6 km depth.

Below Penanggungan volcano, we see a low velocity zone that starts at about 3 km depth and reaches its maximum from 4 to 5 km depth (Figures 9a and 9d). We can further observe a corridor of the low velocity anomaly between the volcano and Lusi (NE-SW direction) starting at approximately 3.5 km depth, which is still visible at 6 km depth (Figures 8c, 9a, and 9d). A low velocity anomaly is also present at a depth of 3 km below the SW part of the Arjuno Welirang complex (Figures 8d–8f and 9e). Its shape is, however, less defined due to the network geometry and the resultant lack of resolution. The first kilometer below the volcanic complex is characterized by a high velocity anomaly (Figures 9a and 9d).

4. Discussion

The purpose of this study is to shed light on the subsurface structure of the region around the Arjuno Welirang complex, Lusi, and the WFS that intersects the two by mapping its shear wave velocity (Vs). Vs are (among other factors) sensitive to the presence of fluids. Hence, using surface waves to invert Vs maps may point out regions with enhanced fluid concentrations and migration.

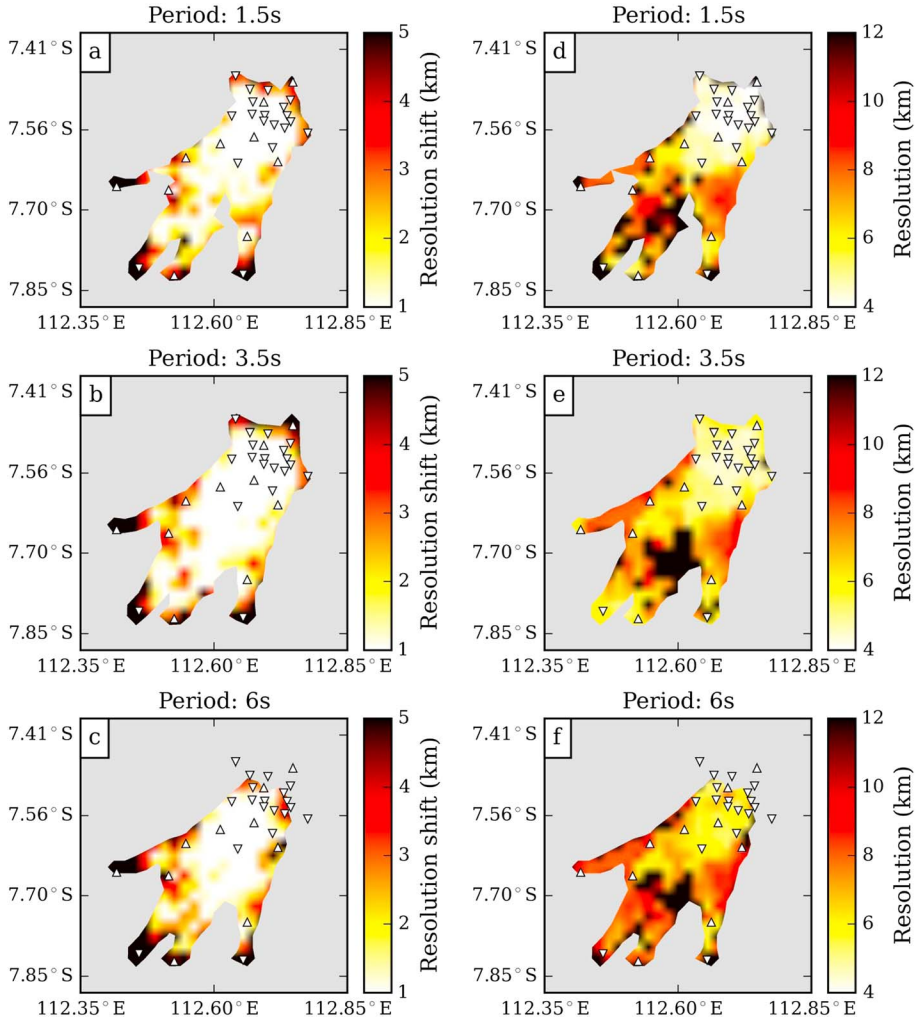

Figure 6. Spatial resolution results. Displacement of the centers of the input spikes after inversion (resolution shift) corresponding to each cell at (a) 1.5 s, (b) 3.5 s, and (c) 6 s. (d–f) The effective diameter of the fitted ellipse that is considered as the maximum reliable anomaly size that the ray coverage is able to resolve. The white triangles denote the seismic station locations.

Our results indicate a complex structure characterized by sharp contrasts of Vs and regions affected by a strong attenuation (Figures 8 and 9). Figure 8a indicates positive velocity anomalies from 10% to 20% in the upper units of the volcanic edifice. We suggest that this may correspond to the interlayering of compacted volcanic sediments and, mostly, lava flows. The high velocity anomaly is suddenly interrupted to the NE by a marked negative anomaly. Such a region is centered on Lusi, suggesting that the elevated presence of fluids may be responsible for the measured large attenuation. Note that the color bar is saturated, suggesting that even larger velocity anomalies are found beneath Lusi. At the surface, such a region is approximately 14 km wide (Figure 9b), and at greater depths, it narrows down to approximately 2 km in diameter (Figure 8c). The Vs anomaly is less pronounced at around 2.5 km depth where anomalies are reduced to about 10%. At around 3 km depth the velocity anomaly increases back up to 20%, until the lower limit of our investigated area. In the cross section (Figures 9a and 9b), the region beneath Lusi appears to have a mushroom shape for which various interpretations may be suggested. Lusi is fed by both organic- and magma-derived fluids erupting at more than 100°C at the surface. We speculate that such strong mushroom-shaped attenuation may be caused by a hydrothermal plume departing from depth and feeding Lusi. By means of basin-scale numerical modeling Lupi et al. (2013, 2014) show that different fluid flow regimes may be occurring in hydrothermal systems, with fast advection processes taking place in the upper part of sedimentary basins, while slower advection may be occurring at greater depths. The funnel shape of

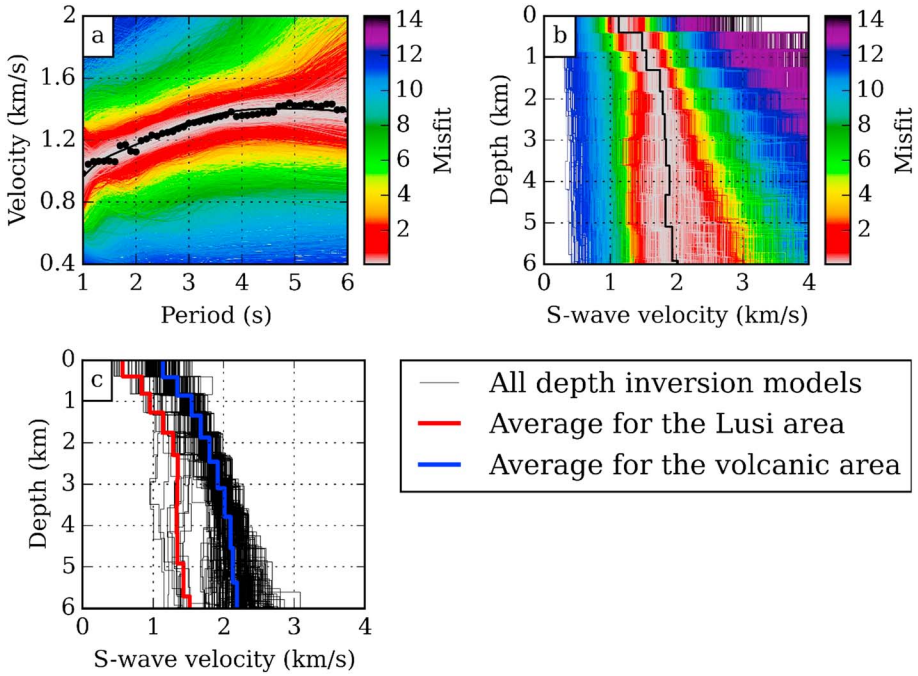

Figure 7. 1-D shear wave velocity profiles. Predicted dispersion curves (a), and randomly generated 1-D velocity profiles (b) for one point in the study area (point B in Figure 5). The black dots in Figure 7a indicate the measured dispersion curve, and the black curve indicates the average of best models. The black line in Figure 7b represents the average of best models. (c) All depth inversion curves (black) and the average for the Lusi area (red) and the average for the volcanic area (blue).

the upper part of the shear wave anomaly beneath Lusi may be related to the rapid advection promoted by the coupling of an elevated geothermal gradient and the higher permeability of the shallow sedimentary units. A second interpretation links the shallow and intense Vs anomaly to the accumulation of shallow hydrocarbon-derived fluids (i.e., oil and gas reservoirs) including the Wunut, Carat, and Tanggulangin gas fields (Istadi et al., 2009) with the slight shear wave variations occurring between ~2 km and 2.5 km depth possibly due to the a low porosity unit (i.e., volcaniclastic deposits) that may retain less fluids (Lupi et al., 2014). Alternatively, the two shear wave anomalies from 0 to 2 km depth and from 2.5 km to 6 km depth may represent the shallow and the deep feeding source, respectively, proposed by Shirzaei et al. (2015) and Mazzini et al. (2017) and first discussed by Mazzini et al. (2012). Despite the possible interpretations associated with the origin of the fluids causing such a marked shear wave anomaly, to the best of our knowledge, Figure 9b is the first image of a crustal hydrothermal plume.

The ANT points toward the occurrence of a well-constrained magmatic reservoir beneath the Penanggungan volcano (Figures 9a and 9d) and a second less certain (due to smearing effects, see spike tests in Figure 5) magmatic reservoir beneath the southern part of the investigated Arjuno Welirang volcanic complex (Figure 9e). We notice a well-developed connection between the magmatic reservoir imaged beneath the Penanggungan volcano and Lusi (Figure 9a). Mazzini et al. (2012) already postulated the presence of an intrusive body feeding Lusi, and the strong NE-striking shear wave anomaly shown in Figures 8d–8f and 9a supports this hypothesis. The NW-SE cross sections (Figures 9d and 9e) show that the interpreted magmatic reservoirs seem to be approximately 6 km wide and subelliptical in shape with vertical elongation. The lateral extensions of such reservoirs seem to be tectonically controlled by the WFS.

Another key feature for the interpretation of the geological setting of the East Java Basin, where Lusi resides, is the narrow low velocity corridor striking NE-SW (Figures 8d–8f) connecting the volcanic complex to the hydrothermal plume feeding Lusi. Such elongated shear wave anomaly corresponds to the suggested location of the WFS (Istadi et al., 2009; Mazzini et al., 2009, 2012). The WFS is a deformation zone characterized by a well-developed damage zone up to ~3 km wide. Fluids migrating at depth (and more specifically from the magmatic bodies that we mapped) may be focused by the high permeability of the damage zone, leading to the measured NE-SW striking low-velocity anomaly. The occurrence of the WFS may also help in interpreting

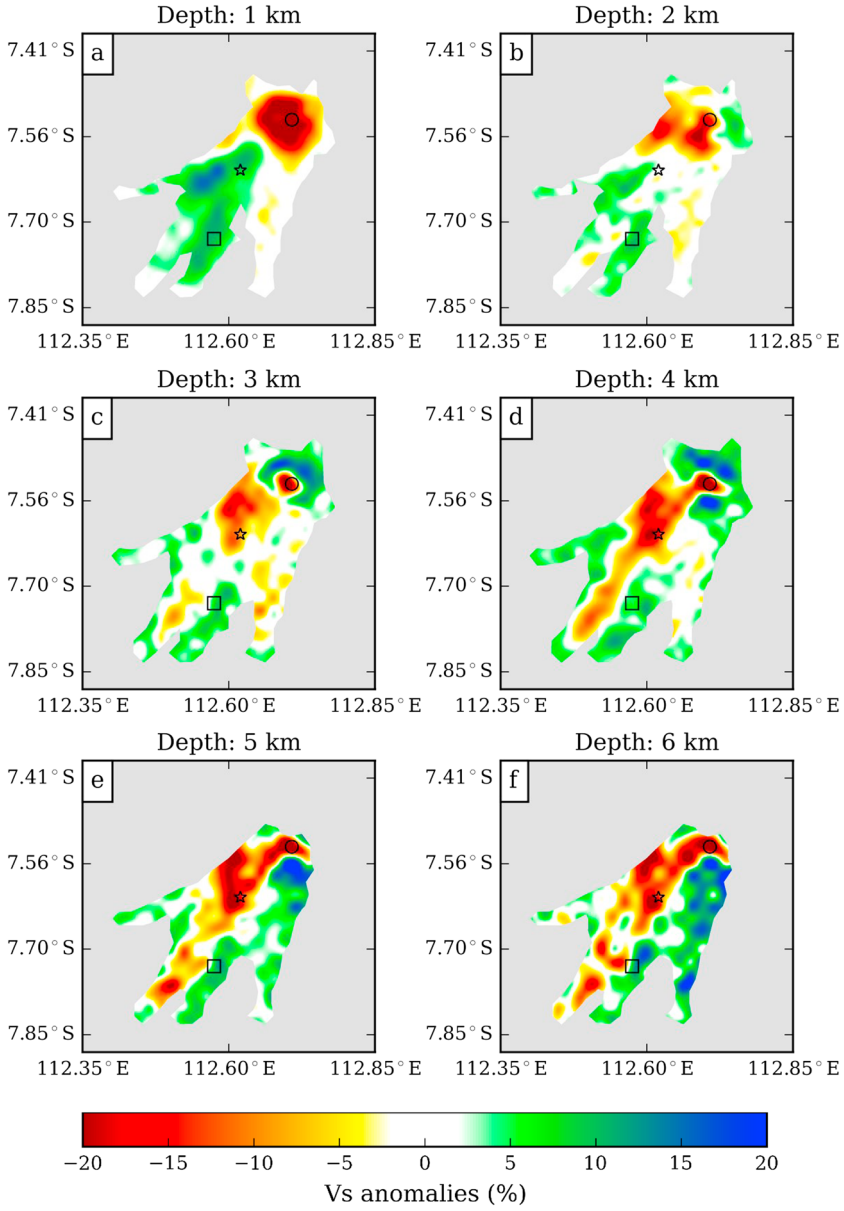

Figure 8. 3-D shear wave velocity model. Horizontal depth slices at (a) 1 km, (b) 2 km, (c) 3 km, (d) 4 km, (e) 5 km, and (f) 6 km. The black symbols are the location of Lusi (circle), summit of Penanggungan volcano (star), and summit of Welirang volcano (square) (shown in Figure 1).

the strong contrast of the velocity anomaly shown in Figure 9c, where at 6 km depth anomalies pass from −20% to 20% in less than 2 km. Our interpretation is also reinforced by geomorphological observations pointing out that in this very same region, the Porong river is abruptly diverted to follow the WFS (Istadi et al., 2009, 2012; Mazzini et al., 2009).

4.1. Implications for the Plumbing System

This study points out that the volcanic complex and Lusi are connected by a NE-striking lineament. This region corresponds to the location of the WFS and is highlighted by the shear wave velocity anomaly shown in Figures 8d–8f. The damaged zones of the WFS may act as a preferential high-permeability pathway, funneling fluid flow from the volcanic complex to the back-arc sedimentary basin. With the obtained tomography we cannot define the composition nor the type of fluids pervading the WFS. However, considering the geological setting (i.e., active volcanic arc) we could speculate that such high-enthalpy fluids have

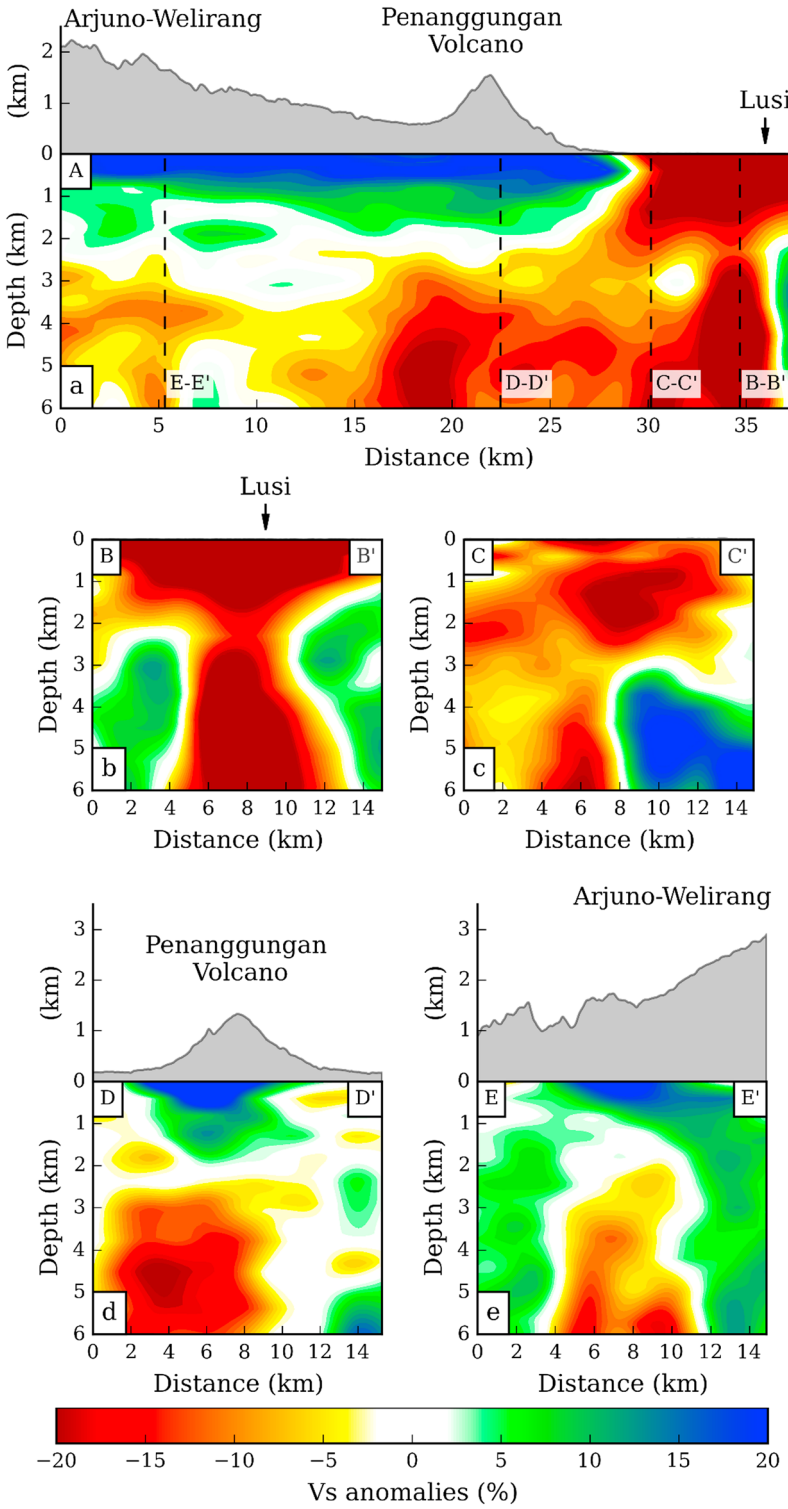

Figure 9. Vertical depth slices (vertically exaggerated ×2) through the 3-D shear wave velocity model. The locations of the slices are indicated in Figure 1. The black dashed lines in AA′ denote the vertical slices BB′, CC′, DD′, and EE′.

been released by the magmatic bodies, as pointed out by our ANT study. The hot fluids (either melt or hydrothermal fluids) moving along these fractured zones could have had (and still have) a massive impact in the organic-rich sediments of the sedimentary basin. Below 4 km, where the most obvious velocity anomaly is observed (Figures 9a and 9b), the regional source rock formation called Ngimbang generated

hydrocarbons for the petroleum province that extends from the onshore back-arc basin to offshore in the Java Sea, Madura Straight, and the Bali Straight (Lelono & Morley, 2011; Mudjiono & Pireno, 2002; Satyana & Purwaningsih, 2003). The total organic carbon content in the Ngimbang Fm varies between 1.6 and 5.7 wt % with coal seams in the lower part that may be as high as 67% (Mazzini et al., 2012; Satyana & Purwaningsih, 2003). As a consequence, the potential for generating carbon gases from the heating of organic matter is remarkable. It is not possible to estimate the timing of such a large-scale fluid migration. However, given that Penanggungan is the youngest (Holocene) volcano of the Arjuno Welirang complex, we suggest that the tomography-imaged hydrothermal fluid migration should be, accordingly, also fairly recent. The distinct Lusi gas signature (Mazzini et al., 2012) indicates that the current baking of the Ngimbang source rock is ongoing at anomalously high temperatures. This corroborates with the finding that the high-temperature fluid migration from the volcanic complex is still ongoing.

5. Conclusions

A dense network of 30 seismic stations has been deployed for 10 months over an area of ~1,000 km^2 covering the region around Lusi, the Arjuno-Welirang volcanic complex, and the Watukosek fault system. The ambient noise Rayleigh wave tomography provides images of the plumbing system feeding Lusi. The obtained shear wave velocity model indicates the presence of a less than 6 km deep hydrothermal plume that reaches the surface at Lusi. This plume is connected at depth to the Penanggungan volcano through a well-defined ~3 km wide low Vs anomaly corridor that extends throughout the investigated region below the depth of ~4 km. This low-velocity narrow zone follows the direction of the Watukosek fault system that strikes the NE of Java at a SW-NE direction. We interpret this corridor as a magmatic intrusion and hydrothermal fluid migration, originating from the volcanic complex and extending toward the NE of the sedimentary basin. This migration uses the weakened rocks along the Watukosek fault system as a preferential pathway. Tomography images combined with sampling and field observations support the scenario that once the hot volcanic fluids reached the source rock, overpressure was generated from the baking of the organic-rich sediments. This mechanism generated a system in critical conditions ready to manifest at surface.

Acknowledgments

The work was funded by the European Research Council under the European Union's Seventh Framework Program grant agreement 308126 (LUSI LAB project, PI A. Mazzini). We acknowledge the support from the Research Council of Norway through its Centers of Excellence funding scheme, project 223272. We thank the Geophysical Instrument Pool Potsdam (GIPP) for providing the instruments for the SEED experiment in the framework of the LUSI LAB project. Matteo Lupi acknowledges SNF for the funding schemes Ambizione (project PZ00P2_154815) and the SCCER-SoE collaborative environment. Anne Obermann acknowledges funding from the European Community Seventh Framework Programme under grant agreement 608553 (Project IMAGE), the Swiss Federal office of Energy with the project GEOBEST, and the SCCER-SoE collaborative environment. BPLS is thanked for their support during field operations. The data presented herein have been collected within the framework of the ERC project 308126. To request the data please contact the Centre of Earth Evolution and Dynamics. The Editor, I. Koulakov, and the anonymous reviewers are thanked for their constructive reviews.

References

Barmin, M. P., Ritzwoller, M. H., & Levshin, A. L. (2001). A fast and reliable method for surface wave tomography. *Pure and Applied Geophysics*, *158*, 1,351–1,375.

Brenguier, F., Shapiro, N. M., Campillo, M., Nercessian, A., & Ferrazzini, V. (2007). 3-D surface wave tomography of the Piton de la Fournaise volcano using seismic noise correlations. *Geophysical Research Letters*, *34*, L02305. https://doi.org/10.1029/2006GL028586

Campillo, M., & Paul, A. (2003). Long-range correlations in the diffuse seismic coda. *Science*, *299*, 547–549. https://doi.org/10.1126/science.1078551

Claerbout, J. F. (1968). Synthesis of a layered medium from its acoustic transmission response. *Geophysics*, *33*(2), 264–269.

Collignon, M., Schmid, D. W., Galerne, C., Lupi, M., & Mazzini, A. (2017). Modelling fluid flow in clastic eruptions: Application to the Lusi mud eruption. *Marine and Petroleum Geology*. https://doi.org/10.1016/j.marpetgeo.2017.08.011

Davies, R. J., Brumm, M., Manga, M., Rubiandini, R., Swarbrick, R., & Tingay, M. (2008). The East Java mud volcano (2006 to present): An earthquake or drilling trigger? *Earth and Planetary Science Letters*, *272*, 627–638.

De Matteis, R., Romeo, A., Pasquale, G., Iannaccone, G., & Zollo, A. (2010). 3D tomographic imaging of the southern Apennines (Italy): A statistical approach to estimate the model uncertainty and resolution. *Studia Geophysica et Geodaetica*, *54*, 367–387.

Gebrande, H. (1982). 3.1.2.3 velocity-density relations. In G. Angenheister (Ed.), *Subvolume B, Landolt-Börnstein—Group V Geophysics*, *chap. Physical Properties of Rocks* (Vol. 1b, pp. 17–20). Berlin: Springer. https://doi.org/10.1007/10201909_4

Istadi, B. P., Pramono, G. H., Sumintadireja, P., & Alam, S. (2009). Modeling study of growth and potential geohazard for LUSI mud volcano: East Java, Indonesia. *Marine and Petroleum Geology*, *26*, 1724–1739. https://doi.org/10.1016/j.marpetgeo.2009.03.006

Istadi, B. P., Wibowo, H. T., Sunardi, E., Hadi, S., & Sawolo, N. (2012). Mud volcano and its evolution. In tech, v. ISBN 978-953-307-861-8, 375–434.

Jaxybulatov, K., Shapiro, N. M., Koulakov, I., Mordret, A., Landès, M., & Sens-Schönfelder, C. (2014). A large magmatic sill complex beneath the Toba caldera. *Science*, *346*, 617–619. https://doi.org/10.1126/science.1258582

Karyono, K., Obermann, A., Lupi, M., Masturyono, M., Hadi, S., Syafri, I., … Mazzini, A. (2017). Lusi, a clastic-dominated geysering system in Indonesia recently explored by surface and subsurface observations. *Terra Nova*, *29*, 13–19. https://doi.org/10.1111/ter.12239

Kennett, B. L. N., Sambridge, M. S., & Williamson, P. R. (1988). Subspace methods for large inverse problems with multiple parameter classes. *Geophysical Journal*, *94*, 237–247.

Kissling, E. (1988). Geotomography with local earthquake data. *Reviews of Geophysics*, *26*(4), 659–698.

Koulakov, I., Serdyukov, A. S., Konovalov, A. V., Mikhailov, V. I., Safonov, D. A., Duchkov, A. A., … El Khrepy, S. (2017). Possible sources of hydrothermal activity and mud volcanism in southern Sakhalin inferred from local earthquake seismic tomography. *Geochemistry, Geophysics, Geosystems*, *18*, 1943–1958.

Koulakov, I., & Shapiro, N. (2015). Seismic tomography of volcanoes. In M. Beer et al., (Eds.), *Encyclopedia of earthquake engineering* (pp. 1–18). Berlin: Springer.

Koulakov, I., Yudistira, T., Luehr, B. G., & Wandono (2009). P, S velocity and Vp/Vs ratio beneath the Toba caldera complex (Northern Sumatra) from local earthquake tomography. *Geophysical Journal International*, *177*, 1121–1139.
Lelono, E. B., & Morley, R. J. (2011). Oligocene palynological succession from the East Java Sea. *Geological Society London, Special Publications*, *355*(1), 333–345.
Levshin, A. L., Yanovskaya, T. B., Lander, A. V., Bukchin, B. G., Barmin, M. P., Ratnikova, L. I., & Its, E. N. (1989). In V. I. Keilis-Borok (Ed.), *Seismic Surface Waves in a Laterally Inhomogeneous Earth*. Dordrecht: Kluwer Academic Puhlishers.
Lobkis, O. I., & Weaver, R. L. (2001). On the emergence of the Green's function in the correlations of a diffuse field. *Acoustical Society of America*, *110*(6), 3011–3017.
Lupi, M., Saenger, E. H., Fuchs, F., & Miller, S. A. (2013). Lusi mud eruption triggered by geometric focusing of seismic waves. *Nature Geoscience*, *6*, 642–646. https://doi.org/10.1038/ngeo1884
Lupi, M., Saenger, E. H., Fuchs, F., & Miller, S. A. (2014). Corrigendum: Lusi mud eruption triggered by geometric focusing of seismic waves. *Nature Geoscience*, *7*, 687–688. https://doi.org/10.1038/ngeo2239
Luzón, F., Almendros, J., & García-Jerez, A. (2011). Shallow structure of Deception Island, Antarctica, from correlations of ambient seismic noise on a set of dense seismic arrays. *Geophysical Journal International*, *185*, 737–748. https://doi.org/10.1111/j.1365-246X.2011.04962.x
Manga, M., Brumm, M., & Rudolph, M. L. (2009). Earthquake triggering of mud volcanoes. *Marine and Petroleum Geology*, *26*, 1785–1798. https://doi.org/10.1016/j.marpetgeo.2009.01.019
Martha, A. A., Cummins, P., Saygin, E., Widiyantoro, S., & Masturyono (2017). Imaging of upper crustal structure beneath East Java-Bali, Indonesia with ambient noise tomography. *Geoscience Letters*, *4*(1), 14. https://doi.org/10.1186/s40562-017-0080-9
Masterlark, T., Haney, M., Dickinson, H., Fournier, T., & Searcy, C. (2010). Rheologic and structural controls on the deformation of Okmok volcano, Alaska: FEMs, InSAR, and ambient noise tomography. *Journal of Geophysical Research*, *115*, B02409. https://doi.org/10.1029/2009JB006324
Mauri, G., Husein, A., Mazzini, A., Irawan, D., Sohrabi, R., Hadi, S., … Miller, S. A. (2017). Insights on the structure of Lusi mud edifice from land gravity data. *Marine and Petroleum Geology*. https://doi.org/10.1016/j.marpetgeo.2017.05.041
Mauri, G., Husein, A., Mazzini, A., Karyono, K., Obermann, A., Bertrand, G., … Miller, S. A. (2017). Constraints on density changes in the funnel-shaped caldera inferred from gravity monitoring of the Lusi mud eruption. *Marine and Petroleum Geology*. https://doi.org/10.1016/j.marpetgeo.2017.06.030
Mazzini, A., & Etiope, G. (2017). Mud volcanism: An updated review. *Earth-Science Reviews*, *168*, 81–112. https://doi.org/10.1016/j.earscirev.2017.03.001
Mazzini, A., Etiope, G., & Svensen, H. (2012). A new hydrothermal scenario for the 2006 Lusi eruption, Indonesia. Insights from gas geochemistry. *Earth and Planetary Science Letters*, *317–318*, 305–318.
Mazzini, A., Nermoen, A., Krotkiewski, M., Podladchikov, Y., Planke, S., & Svensen, H. (2009). Strike-slip faulting as a trigger mechanism for overpressure release through piercement structures. Implications for the Lusi mud volcano, Indonesia. *Marine and Petroleum Geology*, *26*, 1751–1765. https://doi.org/10.1016/j.marpetgeo.2009.03.001
Mazzini, A., Scholz, F., Svensen, H. C., Hensen, C., & Hadi, S. (2017). The geochemistry and origin of the hydrothermal water erupted at Lusi, Indonesia, *Marine and Petroleum Geology*. https://doi.org/10.1016/j.marpetgeo.2017.06.018
Mazzini, A., Svensen, H., Akhmanov, G. G., Aloisi, G., Planke, S., Malthe-Sørenssen, A., & Istadi, B. (2007). Triggering and dynamic evolution of the LUSI mud volcano, Indonesia. *Earth and Planetary Science Letters*, *261*, 375–388. https://doi.org/10.1016/j.epsl.2007.07.001
Miller, S. A., & Mazzini, A. (2017). More than ten years of Lusi: A review of facts, coincidences, and past and future studies. *Marine and Petroleum Geology*. https://doi.org/10.1016/j.marpetgeo.2017.06.019
Mordret, A., Landès, M., Shapiro, N. M., Singh, S. C., & Roux, P. (2014). Ambient noise surface wave tomography to determine the shallow shear velocity structure at Valhall: depth inversion with a neighbourhood algorithm. *Geophysical Journal International*, *198*, 1,514–1,525.
Mordret, A., Landès, M., Shapiro, N. M., Singh, S. C., Roux, P., & Barkved, O. I. (2013). Near-surface study at the Valhall oil field from ambient noise surface wave tomography. *Geophysical Journal International*, *193*, 1,627–1,643.
Mordret, A., Rivet, D., Landès, M., & Shapiro, N. M. (2015). Three-dimensional shear velocity anisotropic model of Piton de la Fournaise Volcano (La Réunion Island) from ambient seismic noise. *Journal of Geophysical Research: Solid Earth*, *120*, 406–427. https://doi.org/10.1002/2014JB011654
Mudjiono, R., & Pireno, G. E. (2002). Exploration of the North Madura Platform, offshore East Java, Indonesia. *Proceedings of the Annual Convention- Indonesian Petroleum Association*, *28*, 707–726.
Nolet, G. (1987). In G. Nolet (Ed.), *Seismic Tomography*. Dordrecht: Springer Netherlands.
Obermann, A., Karyono, K., Diehl, T., Lupi, M., & Mazzini, A. (2017). Seismicity at Lusi and the adjacent volcanic complex, Java, Indonesia. *Marine and Petroleum Geology*. https://doi.org/10.1016/j.marpetgeo.2017.07.033
Obermann, A., Lupi, M., Mordret, A., Jakobsdóttir, S. S., & Miller, S. A. (2016). 3D-ambient noise Rayleigh wave tomography of Snæfellsjökull volcano, Iceland. *Journal of Volcanology and Geothermal Research*, *317*, 42–52.
Olivier, G., Brenguier, F., Campillo, M., Lynch, R., & Roux, P. (2015). Body-wave reconstruction from ambient seismic noise correlations in an underground mine. *Geophysics*, *80*(3), KS11–KS25. https://doi.org/10.1190/geo2014-0299.1
Rawlinson, N., & Sambridge, M. (2005). The fast marching method: An effective tool for tomographic imaging and tracking multiple phases in complex layered media. *Exploration Geophysics*, *36*, 341–350.
Richards, J. R. (2011). Report into the past, present and future social impacts of Lumpur Sidoarjo, Tech. rep., Humanitus Sidoarjo Fund, 1–162.
Ritzwoller, M. H., Lin, F., & Shen, W. (2011). Ambient noise tomography with a large seismic array. *Comptes Rendus Geoscience*, *343*, 558–570.
Rudolph, M. L., Karlstrom, L., & Manga, M. (2011). A prediction of the longevity of the Lusi mud eruption, Indonesia. *Earth and Planetary Science Letters*, *308*, 124–130.
Sambridge, M. (1999). Geophysical inversion with a neighbourhood algorithm—II. Appraising the ensemble. *Geophysical Journal International*, *138*, 727–746.
Satyana, A. H., & Asnidar (2008). Mud diapirs and mud volcanoes in depressions of Java to Madura: Origins, natures, and implications to petroleum system. *Proceedings, Indonesian Petroleum Association*, *2*. IPA08-G-139
Satyana, A. H., & Purwaningsih, M. E. M. (2003). Geochemistry of the East Java Basin: New observations on oil grouping, genetic gas types and trends of hydrocarbon habitats, Proc. Indones. Pet. Assoc. Twenty-ninth Annual Conv. Exhib. Oct. 2003, IPA-G-021.
Sawolo, N., Sutriono, E., Istadi, B. P., & Darmoyo, A. B. (2009). The LUSI mud volcano triggering controversy: Was it caused by drilling? *Marine and Petroleum Geology*, *26*, 1766–1784.
Sethian, J. A. (1996). A fast marching level set method for monotonically advancing fronts. *Proceedings of the National Academy of Sciences of the United States of America*, *93*, 1591–1595.
Sethian, J. A., & Popovici, A. M. (1999). 3-D traveltime computation using the fast marching method. *Geophysics*, *64*(2), 516–523.

Shapiro, N. M., & Campillo, M. (2004). Emergence of broadband Rayleigh waves from correlations of the ambient seismic noise. *Geophysical Research Letters*, *31*, L07614. https://doi.org/10.1029/2004GL019491

Shapiro, N. M., Campillo, M., Stehly, L., & Ritzwoller, M. H. (2005). High-resolution surface-wave tomography from ambient seismic noise. *Science*, *307*, 1615–1618. https://doi.org/10.1126/science.1108339

Shirzaei, M., Rudolph, M. L., & Manga, M. (2015). Deep and shallow sources for the Lusi mud eruption revealed by surface deformation. *Geophysical Research Letters*, *42*, 5274–5281. https://doi.org/10.1002/2015GL064576

Situmorang, B., Siswoyo, Thajib, E., & Paltrinieri, F. (1976). Wrench fault tectonics and aspects of hydrocarbon accumulation in Java, in 5th Annual Convention Proceedings, Indonesian Petroleum Association, 53–67.

Sohrabi, R., Jansen, G., Malvoisin, B., Mazzini, A., & Miller, S. A. (2017). Numerical modeling of the Lusi hydrothermal system: Initial results and future challenges. *Marine and Petroleum Geology*. https://doi.org/10.1016/j.marpetgeo.2017.08.012

Stankiewicz, J., Ryberg, T., Haberland, C., Fauzi, N., & Natawidjaja, D. (2010). Lake Toba volcano magma chamber imaged by ambient seismic noise tomography. *Geophysical Research Letters*, *37*, L17306. https://doi.org/10.1029/2010GL044211

Svensen, H., Iyer, K., Schmid, D., & Mazzini, A. (2017). Modelling of gas generation following emplacement of an igneous sill below Lusi, east Java, Indonesia. *Marine and Petroleum Geology*. https://doi.org/10.1016/j.marpetgeo.2017.07.007

Tanikawa, W., Sakaguchi, M., Wibowo, H. T., Shimamoto, T., & Tadai, O. (2010). Fluid transport properties and estimation of overpressure at the Lusi mud volcano, East Java Basin. *Engineering Geology*, *116*, 73–85.

Thurber, C. H. (1983). Earthquake locations and three-dimensional crustal structure in the Coyote Lake Area, central California. *Journal of Geophysical Research*, *88*(B10), 8,226–8,236.

Tingay, M., Heidbach, O., Davies, R., & Swarbrick, R. (2008). Triggering of the Lusi mud eruption: Earthquake versus drilling initiation. *Geology*, *36*(8), 639–642.

Tromp, J., Tape, C., & Liu, Q., (2005). Seismic tomography, adjoint methods, time reversal and banana-doughnut kernels. *Geophysical Journal International*, *160*, 195–216.

Van Noorden, R. (2006). Mud volcano floods Java. *Nature*. https://doi.org/10.1038/news060828-1

Vanderkluysen, L., Burton, M. R., Clarke, A. B., Hartnett, H. E., & Smekens, J.-F. (2014). Composition and flux of explosive gas release at LUSI mud volcano (East Java, Indonesia). *Geochemistry, Geophysics, Geosystems*, *15*, 2932–2946.

Vanorio, T., Virieux, J., Capuano, P., & Russo, G. (2005). Three-dimensional seismic tomography from P wave and S wave microearthquake travel times and rock physics characterization of the Campi Flegrei Caldera. *Journal of Geophysical Research*, *110*, B03201. https://doi.org/10.1029/2004JB003102

Villagómez, D. R., Toomey, D. R., Hooft, E. E. E., & Solomon, S. C. (2011). Crustal structure beneath the Galápagos Archipelago from ambient noise tomography and its implications for plume-lithosphere interactions. *Journal of Geophysical Research*, *116*, B04310. https://doi.org/10.1029/2010JB007764

Zulfakriza, Z., Saygin, E., Cummins, P. R., Widiyantoro, S., Nugraha, A. D., Lühr, B. G., & Bodin, T. (2014). Upper crustal structure of central Java, Indonesia, from transdimensional seismic ambient noise tomography. *Geophysical Journal International*, *197*(1), 630–635. https://doi.org/10.1093/gji/ggu016